PRELIMINARY STUDY ON THE TENSION-ONLY BRACED SELF-CENTERING STEEL-TIMBER HYBRID FRAME

**Fei Chen[1], Minghao Li[2], Minjuan He[3], Zheng Li[4]**

ABSTRACT: A lateral load resisting system called tension-only braced self-centering steel-timber hybrid frame (TOB-SCSTHF) is proposed. The system utilizes the self-centering steel-timber hybrid joints to provide the self-centering action to the frame. Tension-only braces (TOBs) are used to increase the lateral strength and stiffness of the system. Experimental results on the hybrid joints were taken as the basis to develop the numerical model of the beam-column joints. The model was then extended to the frame model, which was used to explore the hysteretic behavior of TOB-SCSTHF. It was found that the combined use of steel angles in the beam-column joints and the TOBs was efficient in enhancing the structural performance, including the strength, stiffness, energy-dissipation, and the self-centering capability.

KEYWORDS: Steel-timber hybrid joints, Self-centering, Tension-only braces, Lateral performance

1 INTRODUCTION

With the development of engineered wood products (e.g., glued laminated timber, GLT) [1], heavy timber frames have been increasingly used in multi-story buildings. However, heavy timber moment frames are often found to have low stiffness under wind and seismic loads [2]. To increase the lateral stiffness, timber braces can be added to form braced frames. Despite increased stiffness, research has shown braced frames have significant reduction in system ductility and the permanent deformations due to the potential failure of the timber braces and significant residual deformations in the brace end connections. Researchers also attempted to add buckling-restrained braces (BRBs) to GLT frames [3]. Test results revealed that both the stiffness and the ductility of the GLT frames were enhanced. However, the residual deformations of the BRB braced frames were significant.

In this paper, as shown in Figure 1, a lateral load resisting system, TOB-SCSTHF, is proposed. The system consists of two critical components: the self-centering steel-timber hybrid joints (hereafter referred to as hybrid joints) and the tension-only braces. The self-centering capability and lateral stiffness of the system are provided by the hybrid joints and TOBs, respectively. Quasi-static loading tests on two joint specimens were conducted. Further, a numerical model for the hybrid joint was developed within the OpenSees platform. The model was extended to explore the hysteretic response of the TOB-SCSTHF.
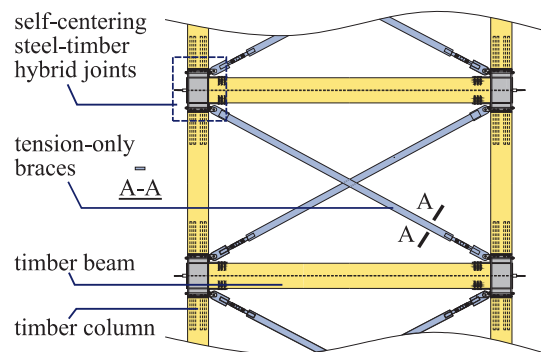
Figure 1 : Tension-only braced self-centering steel-timber hybrid frame (TOB-SCSTHF)

2 CYCLIC TEST ON HYBRID JOINTS

Two hybrid joints were prepared for the cyclic loading test. The details of the test results are available in [2]. A brief introduction of the tests is provided as follows. Two hybrid joint specimens were named Imp-S1 and Imp-S2, respectively. Different from conventional self-centering timber beam-column joints, the hybrid joint used a steel panel in the beam-column interface, as shown in Figure 2 (a). After the post-tensioning of steel tendons, the steel panel resisted the compression from the beam. Glued-in rod (GIR) connections were used to connect the steel panel to the GLT columns. Two-component epoxy resin and grade 4.8 M16 steel rods (each with a slenderness ratio of 25) were used to fabricate the GIR connections. To make a fair comparison, the size of the hybrid joints

[1] Fei Chen, Tongji University, China, chen_fei@tongji.edu.cn
[2] Minghao Li, University of British Columbia, Canada, minghao.li@ubc.ca
[3] Minjuan He, Tongji University, China, hemj@tongji.edu.cn

[4] Zheng Li (Corresponding author), Tongji University, China, zhengli@tongji.edu.cn

was kept the same as that of self-centering timber joint specimens reported in [5]. The initial post-tensioning force for Imp-S1 and Imp-S2 was 54.87 kN and 76.20 kN, respectively. The CUREE loading protocol was used in the test. The moment-rotation curves of the two specimens are shown in Figure 2 (b) and (c). With the use of the steel panel, the gap opening was easy to form in the beam-column interface. As a result, the final failure of two specimens was the fatigue failure of steel angles. Compared with conventional self-centering timber joints, the hybrid joint had higher stiffness, energy-dissipation capability, and connection ductility [4]. The development of the numerical model for the hybrid joint is desired to facilitate further investigation of hybrid joints.
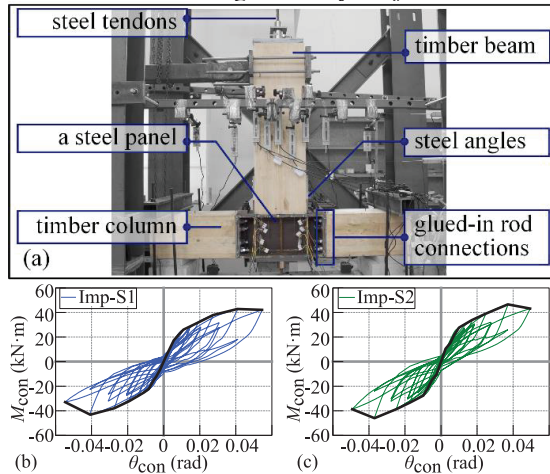

Figure 2 : Cyclic loading test on hybrid joints

3 NUMERICAL SIMULATION ON HYBRID JOINTS

3.1 DETAILED MODEL

The hybrid joint was simulated in OpenSees. There were three key points in the simulation: 1) the modeling of the gap-opening at the timber beam to steel panel interface; 2) the moment-rotation behavior of the GIR connections; and 3) the slip behavior of the self-tapping screws connecting steel angles to the beam.

3.1.1 Modeling of the gap-opening mechanism

As per [6], for self-centering timber joints, the gap-opening mechanism can be simulated with a series of compression-only springs at the beam-column interface. These springs are placed in parallel after being assigned with the Elastic-No Tension (ENT) material property. After post-tensioning, these springs are evenly compressed. The beam-column interface is opened when the edge spring resists zero compression. However, the distributed spring modeling technique might not be ideal in the simulation of the self-centering steel-timber hybrid joint. The reason is that the accumulative damage at the beam end for a hybrid joint is unable to be considered. During the cyclic loading test, permanent compression deformation was observed at the end of the timber beam. After the test, the compression deformation was most obvious at two toes of the beam end. After the gap

opening, the compression force was concentrated into the toe which acted as a rocking pivot. The wood crushing occurred when the GLT compression strength was reached. As a result, the compression stiffness was different for laminations along the height of the beam. The stiffness of the top and bottom laminations degraded faster than that of the inner laminations. The distributed springs with the ENT material however assumed that the springs remained elastic and had no degradation of stiffness, which was different from the test observations. In the paper, the Hyperbolic Gap (HG) material was used for the distributed springs. The HG material is also compression-only. But given compression yield strength F_{ult}, accumulative damage can be considered by HG. The compression stiffness is zero upon a larger compression deformation required for the element with the HG material. Both the strength and stiffness parameters are required in defining the HG material. To determine the strength parameter F_{ult}, the principle of strength equivalence was used. The compression resisted by all springs equaled the compression capacity of the timber beam. Given the rectangular cross-section for the beam, F_{ult} is given by Equation (1). To determine the initial stiffness of the HG material K_{max}, the principle of stiffness equivalence was used with consideration of the end-effect at two ends of the timber beam. As illustrated in Figure 3, the compression stiffness of TB1 was set the same as that of TB2. TB1 corresponded to the beam with two end-effect zones. It can be modelled as three springs in serial. To consider the end effect, two side springs have a reduced axial stiffness represented by $k_{gap}E_{para}/l_e$. TB2 was the beam used in the detailed model for the hybrid joint. TB2 was the beam with only one end-effect zone. One spring connected with a distributed spring model can be used to represent TB2. Assuming the axial stiffness of TB1 equals that of TB2, the initial stiffness K_{max} is obtained with a consideration of the end-effect, as given by Equations (2)-(4).

$$F_{ult} = \frac{f_{para}b_b h_b}{NA_1} \qquad (1)$$

$$K_{max} = k_{end}E_{para} \qquad (2)$$

$$k_{end} = \frac{L_0}{\frac{\lambda+2}{\lambda} \cdot \frac{L_b - 2l_e}{A_b} - \frac{L_b^*}{A_b}} \qquad (3)$$

$$\lambda = \frac{k_{gap}(L_b - 2l_e)}{l_e} \qquad (4)$$

where F_{ult} = yielding compression stress, f_{para} = wood strength parallel to the grain, b_b = beam width, h_b = beam section height, N = number of springs in parallel, A_1 = tributary section area of each spring, A_b = beam section area, k_{end} = reduction factor, k_{gap} = end-effect factor, E_{para} = elastic modulus parallel to the grain, L_0 = length of the offset region, L_b = length of TB1, L_b^* = length of TB2, and l_e = length of the end-effect zone.
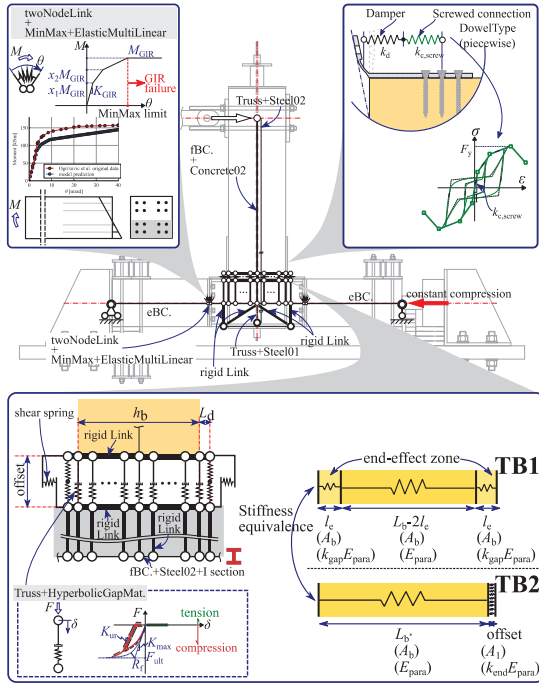
Figure 3 Stiffness equivalence and model illustration

3.1.2 Modeling of the GIR connection

To model the GIR connection, the twoNodeLink element was used to link two overlapped nodes and their degrees of freedom (DOFs) were controlled with the EqualDOF command in OpenSees. Except for the rotational DOF, two translational DOFs of the two nodes were kept the same because only the moment-rotation behavior was modelled. The twoNodeLink element was assigned with ElasticMultiLinear material wrapped with the MinMax material. ElasticMultiLinear material model represented the rotational behavior of GIR connections as a polyline model. The analytical prediction of the GIR connections was conducted based on the model proposed by Ogrizovic et al [7]. The prediction result was in the polyline form and was used as the input for the ElasticMultiLinear material model. The design of GIR connections aimed to ensure that GIR connections had the moment capacity over the possible demand. While the MinMax material was still used to simulate the possible failure of GIR connections. The maximum rotation was specified in the MinMax material. When the relative motion between the two nodes exceeded the limit specified, the MinMax material was activated to fail the ElasticMultiLinear material.

3.1.3 Modeling of the connector between steel angles and beam

The mechanical behavior of self-tapping screws (STSs) connecting steel angles to the timber beam was considered to ensure that the connection stiffness was not overestimated. During the test, the relative slip between one leg of the steel angle and the side face of the timber beam was observed when the gap opening was large. The DowelType model [8] was used to simulate the behavior

of STS connections. The Bezier envelope was used as the backbone curve. Based on the European Yield Model, strength of each STS connection was calculated and used as the input for the DowelType model. The initial stiffness of the STS connections was taken as the minimum value obtained from different STS stiffness models. As per Dong et al. [3], there was a uniform model for the prediction of the shear stiffness k_{ser} of a single inclined STS, as given by Equation (5). The formula was originally proposed by Mirdad et al. [9] for the STS connection between concrete and solid timber. Dong et al. [10] further proved that with the proper selection of the embedment stiffness K_h and the withdrawal stiffness K_{ax} per unit area, the equation was also applicable in calculating the stiffness of the STS connection between the steel member and the GLT member. As per Equation (5), the contribution of the withdrawal stiffness to the total lateral stiffness of STS connections is zero when the angle between the axis of a single STS and the grain direction is 90 degrees. As given by Equations (6)~(8), three different formulas of K_h were used to calculate the lateral stiffness of STS connections. The lowest value among the three prediction results was taken as the input for the initial stiffness of the DowelType model. k_{ser} was calculated to be 992 N/mm. Other material parameters were adopted as the values suggested in [8].

$$k_{ser} = \frac{3E_{STS}Id\left[2\left(3l_f + 2l_{ef}\right)K_{ax}\pi l_{ef}\left(\cos^2\theta + 0.5\mu_f\sin2\theta\right)\right]}{6E_{STS}I\left(3l_f + 2l_{ef}\right) + K_h dl_{ef}^2 l_f^3 \sin^2\theta}$$
$$+ \frac{3E_{STS}IdK_h l_{ef}^2\left(\sin^2\theta - 0.5\mu_f\sin2\theta\right)}{6E_{STS}I\left(3l_f + 2l_{ef}\right) + K_h dl_{ef}^2 l_f^3 \sin^2\theta} \tag{5}$$

$$K_h = \frac{0.00011\rho_m^{2.443}d^{-0.956}}{7.663\cos^2\theta + 2.645\sin^2\theta} \tag{6}$$

$$K_h = \frac{\left(0.22 + 0.014d\right)\rho_m d^{-1}}{1.17\sin^2\theta + \cos^2\theta} \tag{7}$$

$$K_h = \frac{2\rho_m^{1.5}\dfrac{d_{ef}}{23}}{dl_{ef}} \tag{8}$$

where E_{STS} = elastic modulus of STS, $I = \pi d^4/64$ the moment of inertial of the STS, d = nominal diameter of the STS, l_f = free length of the STS, l_{ef} = effective penetration length of the STS, θ = angle between the axis of STS and the direction of the wood grain, μ_f = friction coefficient, ρ_m = mean value of the wood density, d_{ef} = effective diameter of the STS.

3.1.4 Comparison against experimental results

The comparison between the numerical simulation results and experimental results was shown in Figure 4. The hysteretic curves from the simulation and the test recording are overlapped in the first two subfigures. The model prediction agreed well with the test results in terms of both the strength and the residual deformation. However, the decompression point of the model was lower than that of the test. One possible reason was that the stiffness degradation of the springs at the beam-column interface was severe than in the real situation. After a few cycles of loading, the two side springs had significant stiffness degradation and could not support the rocking of the beam. Inner springs then picked up the load

and acted as the rocking pivot. As a result, the decompression point was slightly lower than the test results. The numerical model also performed well in predicting the variation of the post-tensioning force and energy dissipation, as shown in Figure 4 (c)~(f).
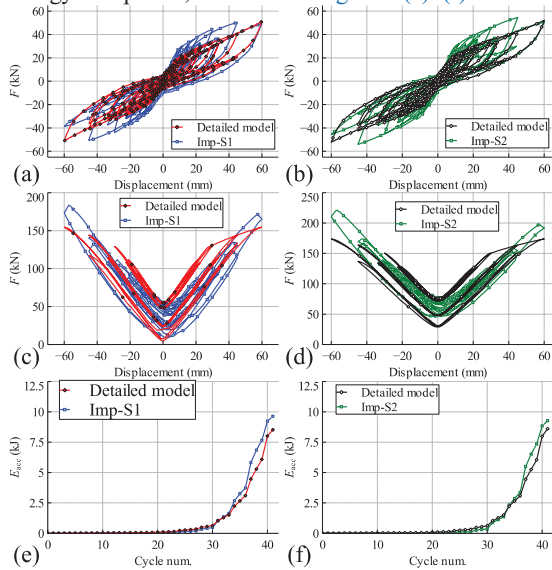

Figure 4 : Numerical simulation against experimental results

3.2 PHENOMENOLOGICAL MODEL

The integration of the aforementioned detailed model into the frame model might be difficult due to the complexity of the joint model. To avoid the convergence problem, a phenomenological model was further developed for the hybrid joints. To mimic the hysteretic behavior of hybrid joints, SelfCentering and DowelType materials were combined in parallel as the candidate material for the phenomenological model. The number of parameters required for SelfCentering and DowelType material was 4 and 17, respectively. The genetic algorithm was used to build the automatic calibration process for the phenomenological model. NSGA-II [11] was selected to conduct the multi-objective optimization. One of the desirability functions is given by Equation (9). The function F_1 was used to ensure that the force-displacement curve of the simulation results match the test results. In addition, the second desirability function F_2 was defined in terms of energy dissipation, as given by Equation (10). Constrained by F_2, the model error of the accumulative energy dissipation was expected to be controlled.

$$F_1 = \sum_{i=1}^{n} \omega_i \left(F_{it} - F_{im} \right)^2 \qquad (9)$$

$$F_2 = \sum_{i}^{n} \frac{\left| E_{it} - E_{im} \right|}{\left| E_{it} \right|} \qquad (10)$$

where $\omega_i, i=1\sim n$ = the weight factor for the ith data point, F_{it} = target force of the ith data point, F_{im} = model force of the ith data point, E_{it} = target energy dissipated upon the ith data point, E_{im} = model energy dissipated upon the ith data point.

The flowchart of the parameter calibration process is shown in Figure 5. To ensure that the optimized parameters can be obtained, the number of generations was 20. It means that the set of parameters was obtained after 20 times of evolution. Within each round of evolution, the number of candidates was 5000. For each candidate, the value of each model parameter was randomly set within the rational range. The final results were obtained after the comparison between 10000 (20 times 5000) combinations of parameters. More than one set of parameters was available after the multi-objective optimization. All the final outputs were non-dominated solutions, which meant each of them, i.e., one set of parameters, was a suitable compromise to minimize both desirability functions.
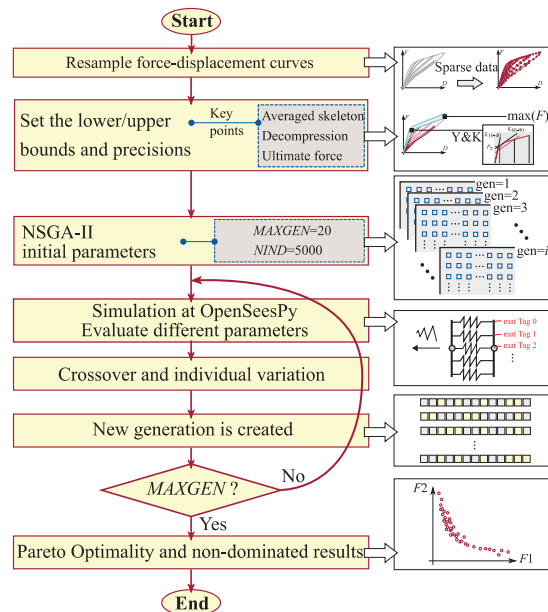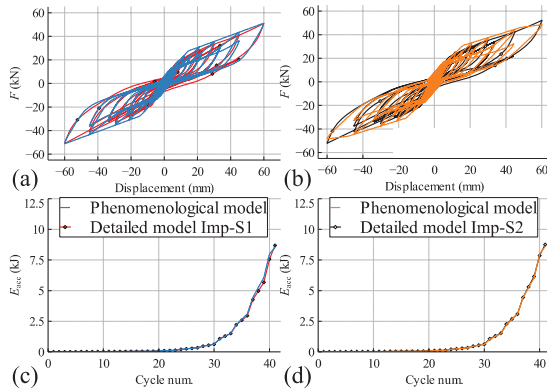

Figure 5 : Flowchart for determining the optimized parameters for the phenomenological model

Taking one of the non-dominated solutions to make the simulation in OpenSees, the prediction from the phenomenological model was presented in Figure 6, together with the results from the detailed model. The comparison validated the accuracy of the phenomenological model. The model was then integrated into the frame model in the next section.

Figure 6 : Flowchart for determining the optimized parameters for the phenomenological model

4 NUMERICAL SIMULATION OF TOB-SCSTHF

The hysteretic behavior of TOB-SCSTHF was explored based on the phenomenological model of the hybrid joint. The modeling method of TOBs is first introduced and validated against theoretical solutions. It is then followed by the numerical simulation on TOB-SCSTHF with or without steel angles installed at the beam-column joints.
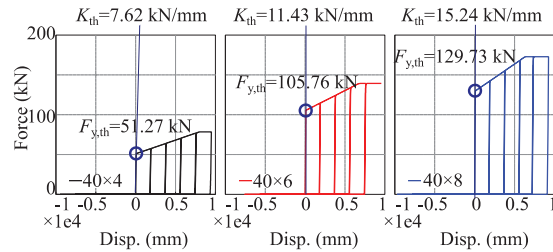
4.1 MODELING OF TOBs

Compared with common steel braces, TOB is characterized as a steel brace with negligible compression resistance. It is expected that TOBs provide zero resistance to the self-centering frame during the load reversal. An equivalent model was proposed for TOBs by Ying et al. [12] in ABAQUS. The modeling technology was recreated within OpenSees. As shown in **错误!未找到引用源。**, the model has four truss elements connected end to end.
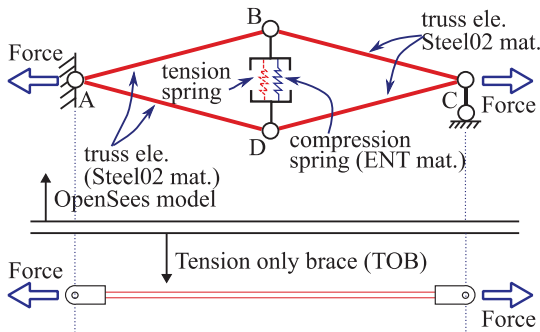
Figure 7 : OpenSees model for a single TOB

Nodes A and C are the two ends of a single TOB. When the TOB is in tension, nodes A and C depart from each other, and element BD is under compression. When the TOB is in compression, nodes A and C are getting closer and the element BD is in tension. Element BD is assigned with two materials in parallel: ENT and Elastic material. ENT material is a compression-only material and Elastic material has a close to zero tension stiffness. So element BD can resist compression only. When the TOB model is

under tension along the AC axis, element BD resists the compression, so the TOB model has the tension stiffness. The TOB model has no compression resistance because the BD element has zero tension stiffness.

The TOB with the flat bar was simulated by using the TOB model. Under the reversed cyclic loading, the hysteretic curves of TOBs with three different thicknesses (4/6/8 mm) were obtained. The simulation results are shown in Figure 8. The analytical prediction on the yielding force and the initial stiffness of a single TOB were also annotated in Figure 8. The satisfactory agreement validated the modeling method for TOBs.

Figure 8 : Numerical predictions on the TOBs with different thickness

4.2 MODELING OF TOB-SCSTHF

Both the hybrid joint model and the TOB model were integrated into the OpenSees model for TOB-SCSTHF. The basic geometry and material information of the frame are listed in Figure 9.
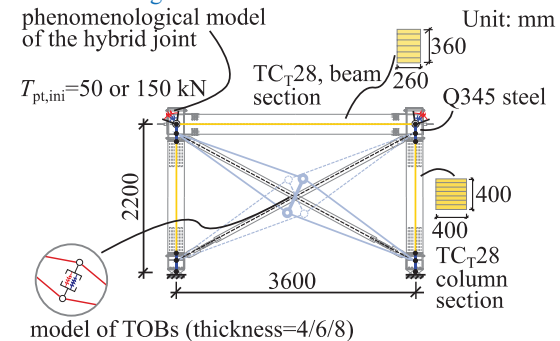
Figure 9 : Numerical model of TOB-SCSTHF

Five numerical models were built corresponding to the five TOB-SCSTHFs listed in Table 1.

Table 1 : Information of five TOB-SCSTHF models

Model ID	TOB[a]	$T_{pt,ini}$ (kN)	Steel angles at beam-column joints
M1	40×4	50	w/o
M2	40×6	50	w/o
M3	40×8	50	w/o
M4	40×4	150	w/[b]
M5	40×6	150	w/[c]

[a] Numbers represent cross-sections of TOB in mm;
[b] The steel angles had reduced thickness of 7 mm;
[c] The steel angles had reduced thickness of 5 mm.

TOBs with three thicknesses were used in the same SCSTHF ($T_{pt,ini}$=50 kN, without steel angles). The hysteretic curves of the three TOB-SCSTHFs are shown in Figure 10 (a). The hysteresis of the TOB-SCSTHF was in a flag shape and almost zero residual deformation was found when the lateral force was zero. The stiffness and strength of the SCSTHF were enhanced along with the increase in the thickness of TOBs. At the same time, the difference in TOBs used in the frame didn't change the residual deformation. All three frames had a full re-centering after the cyclic loading. Without the degradation of the self-centering capability, TOBs can be used when SCSTHF has insufficient lateral strength or stiffness. The introduction of TOBs into SCSTHF also changed its energy dissipation capability. As shown in Figure 10 (b), there is a plateau on the curve of accumulative energy. When no beam-column dampers are used in the SCSTHF, TOBs are the only component dissipating energy. The plastic deformation and the related energy dissipation can only happen within the first loading cycle if multiple loading cycles with the same loading amplitude was applied to the TOBs. After the first loading cycle, the TOB is elongated due to plastic deformation. It means that a larger deformation is required to make the TOB under tension again. To increase the energy dissipation of TOB-SCSTHF, steel angles were installed at the beam-column joints. Two models with steel angles were simulated and their responses are shown in Figure 10 (c). Their hysteretic curves were still in the flag shape and an increase in the residual deformation was also noticed. The increase was due to the use of steel angles. Since the use of TOBs had no influence on the self-centering performance of the frame, the installation of the steel angles was a compromise solution to the frame. The accumulative energy dissipation curves of the two new frames were shown in Figure 10 (d). Owing to the energy dissipation by the steel angles, a continuous increase is observed in the two curves. It means that the combined use of steel angles and TOBs in SCSTHF is a promising solution when there is a requirement for different structural aspects, including strength, stiffness, energy-dissipation, and residual deformations.
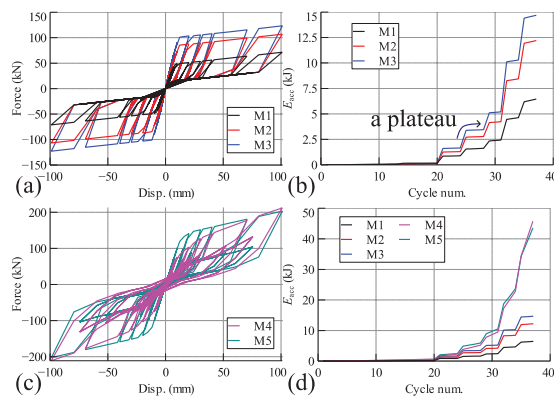

Figure 10 : Hysteretic responses of TOB-SCSTHF with or without steel angles

5   CONCLUSIONS

This paper presents a preliminary study on the hysteretic performance of a new lateral load resisting system called TOB-SCSTHF for heavy timber frames. The cyclic test on the hybrid beam-column joints proved their capability to provide sufficient re-centering action to the frame. Based on the experimental results, both detailed and phenomenological models were developed for the hybrid joints. The joint model was then integrated into the numerical model of TOB-SCSTHF. The simulation results showed that the introduction of TOBs increased the lateral resistance and stiffness of the frames. Being different from the BRBs, the use of TOBs did not impair the self-centering capability.

REFERENCES

[1] Sun X., He M., and Li Z. Novel engineered wood and bamboo composites for structural applications: State-of-art of manufacturing technology and mechanical performance evaluation. Construction and Building Materials, 249, 118751, 2020.

[2] Shu Z., Ning B., Chen J., Li Z., He M., Luo J., and Dong H. Reinforced moment-resisting glulam bolted connection with coupled long steel rod with screwheads for modern timber frame structures. Earthquake Engineering & Structural Dynamics, 2022.

[3] Dong W., Li M., Lee C. L., MacRae G., and Abu A.: Experimental testing of full-scale glulam frames with buckling restrained braces. Engineering Structures, 222, 111081, 2020.

[4] Li Z., Chen F., Sun X., Shu Z., and He M.: Hysteretic performance of self-centering glulam beam-to-column connections with steel core panel zone. *International Conference on Green Building, Civil Engineering and Smart City*, pages 893-900. Springer, Singapore, 2023.

[5] Li Z., He M., and Wang K.: Hysteretic performance of self-centering glulam beam-to-column connections. Journal of Structural Engineering, 144(5), 04018031, 2018.

[6] Granello G., Palermo A., Pampanin S., Pei S., and Van De Lindt J.: Pres-lam buildings: state-of-the-art. Journal of Structural Engineering, 146(6), 04020085, 2020.

[7] Ogrizovic J., Wanninger F., and Frangi A.: Experimental and analytical analysis of moment-resisting connections with glued-in rods. Engineering Structures, 145, 322-332, 2017.

[8] Dong H., He M., Wang X., Christopoulos C., Li Z., and Shu, Z.: Development of a uniaxial hysteretic

model for dowel-type timber joints in OpenSees. Construction and Building Materials, 288, 123112, 2021.

[9] Mirdad M. A. H., and Chui Y. H.: Stiffness prediction of mass timber panel-concrete (MTPC) composite connection with inclined screws and a gap. Engineering Structures, 207, 110215, 2020.

[10] Dong W., Li M., Lee C. L., and MacRae G.: Numerical modelling of glulam frames with buckling restrained braces. Engineering Structures, 239, 112338, 2021.

[11] Deb K., Pratap A., Agarwal S., and Meyarivan, T. A. M. T.: A fast and elitist multiobjective genetic algorithm: NSGA-II. IEEE transactions on evolutionary computation, 6(2), 182-197, 2002.

[12] Yin H., and Shi G.: Finite element analysis on the seismic behavior of fully prefabricated steel frames. Engineering Structures 173: 28-51, 2018.